

pubs.acs.org/JCTC Article

Fast, Faithful Simulations of Donor-Acceptor Interface Morphology

Puja Agarwala, Enrique D. Gomez, and Scott T. Milner*



Cite This: J. Chem. Theory Comput. 2022, 18, 6932-6939



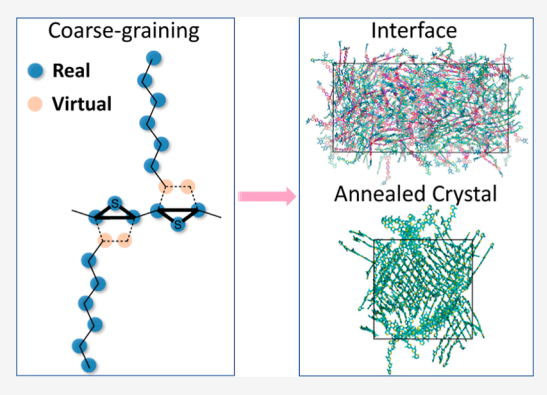
ACCESS

Metrics & More

Article Recommendations

Supporting Information

ABSTRACT: The local structure of conjugated polymers governs key optoelectronic properties, such as charge conduction and photogeneration at donor—acceptor interfaces. Because conjugated polymers are large, stiff, and relax slowly, all-atom molecular dynamics simulations are computationally expensive. Here, we describe a coarse-graining method that exploits the stiffness of constituent aromatic moieties by representing each moiety as rigidly bonded clusters of atoms wherein virtual sites replace several atoms. This approach significantly reduces the degrees of freedom while faithfully representing the shape and interactions of the moieties, resulting in 10 times faster simulations than all-atom simulations. Simulation of a donor polymer (P3HT) and a non-fullerene acceptor (O-IDTBR) validates the coarse-graining method by comparing structural properties from experiments, such as the density and persistence length. The fast simulation produces equilibrated



systems with realistic morphologies. The simulation results of an equimolar mixture of P3HT, with a molecular weight of 1332 g mol⁻¹, and an O-IDTBR mixture suggest that the interface width must be larger than 7 nm. Also, we investigate the effect of slow cooling on morphologies, particularly the number of close contacts that facilitates carrier transport. Slow cooling increases close contacts, and the effect is more pronounced in crystal-forming P3HT than in O-IDTBR, where bulky side-groups hinder crystal formation.

1. INTRODUCTION

The flexibility, lightweight, and transparency of organic photovoltaic cells (OPVs) may lead to numerous applications, such as power-generating windows, electronic textiles, synthetic skin, and space applications. To improve the efficiency of an OPV, the donor—acceptor morphology should have an optimal domain size for exciton diffusion, maximum interfacial area for charge separation, and an interpenetrating network for charge extraction. The efficiency depends not only on the mesoscopic morphology at the donor—acceptor interface but also on the local conformation and packing of polymer chains.

At the donor—acceptor interface, charge separation and charge recombination compete; minimizing recombination reduces voltage loss and improves the OPV efficiency. This recombination loss depends on the energy of the charge transfer (CT) state and the electronic coupling ($t_{\rm LE-CT}$) between the CT state and the lowest local excited (LE) state, which is sensitive to local molecular conformations at the interface. Also, the interface width, or the fraction of the mixed region, in a bulk heterojunction (BHJ) impacts the performance of OPVs. Therefore, characterizing the local morphology of the interface is an essential step toward developing efficient OPV materials and devices.

Various approaches, such as bandgap engineering, side-chain engineering, and device design modifications, have been employed to improve the OPV efficiency. $^{10-12}$ They character-

ize the device morphology by experimental techniques such as grazing-incidence wide-angle X-ray scattering, transmission electron microscopy, atomic force microscopy, scanning electron microscopy, and neutron reflectometry. These studies connect morphology with the device efficiency; however, characterization of the donor—acceptor interface remains a challenge that hinders OPV design efforts.

Molecular dynamics (MD) simulation can provide a nanoscale view of the donor—acceptor interface. Huang and others have studied semiconducting polymer morphologies using all-atom and coarse-grained MD simulations. ^{17–22} However, all-atom simulations of large, stiff, and slow relaxing semiconducting polymers are computationally expensive.

For instance, Kupgan et al. used an all-atom simulation to study the morphology of the PTB7-Th polymer with various non-fullerene acceptors (NFAs).²⁰ Optimistically, the authors assumed that the system equilibrates within 30 ns because the density and total energy converge to a constant value. However, this is not long enough for any but the most local features of blend morphology to relax, as we shall show below.

Received: May 6, 2022 Published: October 11, 2022





One way to accelerate equilibration is coarse-graining. For example, Huang et al. coarse-grained each monomer of poly(3-hexylthiophene-2,5-diyl) (P3HT) and phenyl-C61-butyric acid methyl ester into a single bead to study its morphology. However, a severe shortcoming of this approach is that it cannot represent the planar structure and the dipole moment of P3HT monomers, which dictate the interchain charge transfer rate. In addition, key details of molecular conformation that govern CT state energies are not represented.

In this work, we develop an efficient method of coarsegraining that reduces the simulation time while retaining the shape and interactions of the monomers in stiff conjugated polymers. We take advantage of the stiffness of the constituent aromatic moieties by representing them as a cluster of rigidly bonded atoms and replacing several atoms with virtual sites. This approach reduces the degrees of freedom and significantly improves the simulation efficiency.

We apply this new coarse-graining approach to a commonly studied donor polymer, P3HT. We validate our simulation by comparing to the experimentally obtained persistence length and melt density. We extend the method to study a nonfullerene acceptor oligomer, (5Z,5'Z)-5,5'-((7,7'-(4,4,9,9-tetraoctyl-4,9-dihydro-s-indaceno [1,2-b:5,6-b'] dithiophene-2,7-diyl) bis (benzo[c][1,2,5] thiadiazole-7,4-diyl)) bis (methanylylidene)) bis(3-ethyl-2-thioxothiazolidin-4-one) (O-IDTBR), which we validated by comparing the simulated crystal density to the experimental one.

Using our fast simulation method, we obtain realistic morphologies for the P3HT/O-IDTBR interfacial region. We demonstrate the role of the side-group architecture by comparing the effect of bulky O-IDTBR side-groups and the more evenly distributed P3HT side-groups on the probability of close contact between moieties. Our results reveal that the out-of-plane attachment of the O-IDTBR side-group sterically hinders π – π stacking, whereas the in-plane attachment of the P3HT side-group does not.

We also study the effect of slow cooling on morphology. Experimentally, annealing alters the morphology of donor—acceptor blends. ^{27,28} Our fast simulation techniques allow us to explore such morphological changes qualitatively. We anneal each pure system and the blend from 600 to 300 K over 600 ns and compare the resulting morphology with a system quenched to 300 K. We find that such annealing increases the number of close contacts between monomers, relevant to interchain charge transport.

2. VIRTUAL-SITE COARSE-GRAINING

Coarse-graining increases the simulation efficiency by reducing the degrees of freedom. In one approach, a group of atoms is represented by one bead. For example, each ring in a molecule consisting of stiff rings can be represented by a single bead. However, a reduction in degrees of freedom always entails some loss of information. A stiff ring represented as a bead loses its planar structure and dipole moment, which play a vital role in interchain interactions. Therefore, we develop a coarse-graining approach that increases the simulation efficiency while retaining the shape and interactions of constituent moieties.

The focus of our study is conjugated polymers consisting of aromatic rings as repeat units. Aromatic rings are stiff, so the relative position of atoms in the ring does not vary significantly. Therefore, we dispense with the slight variation in bonds, angles, and dihedrals within a monomer and consider

them fixed. This allows us to reduce the number of independently moving particles by replacing some real atoms with virtual sites.

GROMACS provides a way to define virtual interaction sites, which have defined positions relative to real atoms. A virtual site does not move independently but contributes to non-bonded forces as for real atoms. The mass of the virtual site is distributed among nearby real atoms. Therefore, we do not lose any critical information by replacing real atoms in stiff moieties with virtual sites.

Our strategy to coarse-grain an aromatic ring is as follows. First, we represent three atoms describing the plane of the ring as real atoms and the rest of the atoms as virtual sites, as shown

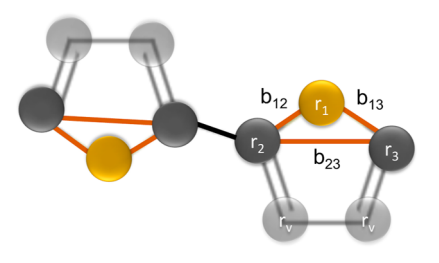


Figure 1. Aromatic rings with real atoms (dark), fixed bonds (red), and virtual sites (light).

in Figure 1. The virtual site position r_v is given in terms of real atom position r_i by

$$r_{\rm v} = \sum_{i=1}^3 w_i r_i \tag{1}$$

in which w_i are scalars, $w_1 = 1 - a - b$, $w_2 = a$, and $w_3 = b$, with a and b chosen to reproduce the ideal monomer geometry. The ideal monomer geometry is an energy-minimized structure computed using density functional theory with the B3LYP functional and the 6-31G basis set in Gaussian. ¹⁹

The virtual site mass $m_{\rm v}$ is distributed to neighboring real atoms with mass $m_{\rm r}$ such that the final mass of the real atom $m_{\rm R}$ becomes

$$m_{\rm R} = m_{\rm r} + \frac{\sum m_{\rm v}}{3} \tag{2}$$

Fixing the bond lengths b_{ij} between real atoms as in Figure 1 likewise fixes all the angles and dihedrals within the ring, which further reduces the degrees of freedom. For example, in a thiophene dimer, as shown in Figure 1, the number of atoms, bonds, angles, and dihedrals is drastically reduced by the virtual site method of coarse-graining, as enumerated in Table 1. For other polymers and oligomers with stiff moieties, the degree of freedom reduction will depend on the number of aromatic rings.

For an MD simulation, we require bonded and non-bonded forcefield parameters. We obtain the non-bonded Lennard-Jones parameters from the optimized potentials for liquid simulations (OPLS) database.³⁰ We evaluate the charges and bonded parameters using density functional theory with the B3LYP functional and the 6-31G basis set. Partial charges are determined using electrostatic fitting.¹⁹ The bond, angle, and dihedral between adjacent monomers are not constrained, so bonded potentials are required for these interactions. We determine these by performing scans in Gaussian.

Table 1. Degrees of Freedom of a Thiophene Dimer Shown in Figure 1

type	all-atom	united atom	virtual site
atoms	16	10	6
bonds	17	11	1
constraints	0	0	10
angles	26	14	2
dihedrals	20	14	3
total	79	49	22

We calculate the bond-stretching potential by stretching the bond around the minimum bond length b_{ij} , with a rigid scan such that every other bond, angle, or dihedral remains fixed. We fit the resulting energy versus bond length to a harmonic potential $V_{\rm b}(r_{ij}) = 1/2k_{ij}^{\rm b}(r_{ij}-b_{ij})^2$ to obtain the bond spring constant $k_{ij}^{\rm b}$. Similarly, to obtain the angle spring constant $k_{ijk}^{\rm o}$, we perform a rigid scan of the angle around the minimum angle $\theta_{ijk}^{\rm o}$ and fit the result to a harmonic potential $V_{\rm a}(\theta_{iik}) = 1/2k_{iik}^{\rm o}(\theta_{iik}-\theta_{ijk}^{\rm o})^2$.

We obtain the improper and proper dihedral potential parameters with a similar method. The dihedral potential obtained from such a scan includes the 1–4 Lennard-Jones (LJ) interaction. However, the OPLS conventions for dihedral interaction partially exclude this LJ interaction. Hence, to obtain a dihedral potential with this convention, the 1–4 LJ interaction is determined by evaluating the energy of each scanned configuration, which is then subtracted from the DFT energy. We fit the difference to a Ryckaert–Bellemans function $V_{\rm rb}(\phi_{ijkl}) = \sum_{n=0}^5 C_n (\cos(\phi_{ijkl}))^n$ to obtain the parameter C_n . We have evaluated potential parameters for P3HT and O-IDTBR, which are listed in Sections S3 and S4 of Supporting Information.

In GROMACS and other simulation platforms, each molecular structure to be simulated requires a topology file, which supplies the constituent atom properties and the bond, angle, and dihedral interactions. Writing such a file by hand is tedious for large molecules. GROMACS supplies a utility pdb2gmx, designed for proteins but applicable to polymers, which automates this task. Unfortunately, pdb2gmx generates all possible bonded interactions, notably including a large number of dihedral interactions. In contrast, part of the efficiency of our approach arises from generating the absolute minimum set of bonded terms. Therefore, we pursue an alternate approach; we write by hand an .itp file for each monomer, designed such that a single Python script can readily assemble these files for a long chain. We describe this approach in more detail in Section S1 of Supporting Information.

2.1. Coarse-Graining Validation. Any simulation method must be validated against experiments to ensure realistic results. For our study of P3HT and O-IDTBR, we simulate each pure system and compare the results with experimental properties. For P3HT, we compare the melt density and chain persistence length in experiment. The density depends on the non-bonded parameters, and the persistence length depends on the dihedral potential; thus, a favorable comparison to the experiment gives confidence in these potential parameters. For O-IDTBR, we simulate the O-IDTBR crystal and compare its density and structure with experiment.

2.1.1. Pure P3HT. Our simulated melt consists of 96 regioregular P3HT oligomers of 8 monomers each. The system consists of 72 real atoms and 16 virtual sites per molecule. The

details of constraints and potential parameters are listed in Section S3 of Supporting Information. In the initial configuration, molecules are placed in all-trans conformations in a regular array at a low density in a simulation box with periodic boundary conditions, as shown in Figure 2a. To

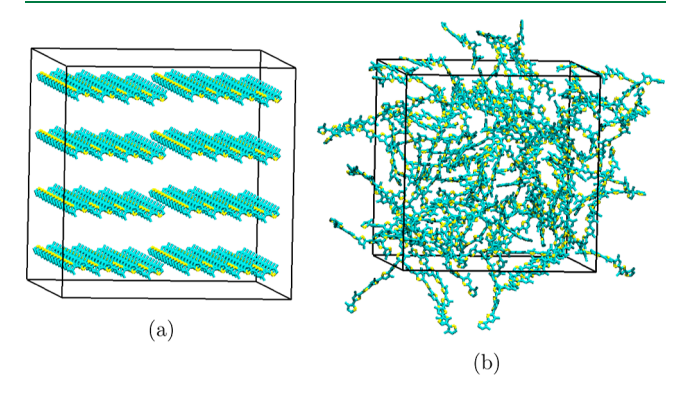


Figure 2. (a) Initial and (b) equilibrated configurations of P3HT melt (side-groups not shown).

equilibrate, we minimize the energy, resize it to the approximate melt density in a 5 ns simulation, and finally simulate for 300 ns at 600 K and 1 atm. The simulation time step is 4 fs, and we use the velocity rescaling thermostat and Berendsen barostat for temperature and pressure control, respectively. The NPT simulation is 5 times longer than the time required for a molecule to diffuse its own radius of gyration. Figure 2b shows a snapshot of the equilibrated system.

Our coarse-grained simulations run 10 times faster than conventional all-atom simulations. The P3HT simulation described above runs at 300 ns/day with GPU acceleration and four processors; the all-atom simulation with an equivalent system and hardware runs at 30 ns/day.³¹ The all-atom simulation has the same temperature and pressure control as the virtual site simulation and uses a 1 fs simulation time step. In comparison, our virtual site simulation uses a 4 times larger time step and 5 times fewer degrees of freedom. We conclude that the 4-fold increase in time step boosts the simulation speed by a factor of 4, and the 5-fold reduction in degrees of freedom boosts the simulation speed by a factor of about 3.

We simulate the system at 600 K to take advantage of faster dynamics at high temperatures to obtain an equilibrated isotropic melt. To validate our results, we compare the simulated melt density with experiments. The equilibrated P3HT system has a melt density of 0.91 g/cm³ at 600 K. Real P3HT degrades at 600 K; so, to compare, we extrapolate the experimental density obtained by Zhan et al. for regiorandom P3HT, which is amorphous for a large temperature range. The extrapolated density of 0.93 g/cm³ agrees with the simulation.

We also compare the persistence length $l_{\rm p}$ of P3HT from simulation with experimental results of McCulloch et al. ²⁶ We evaluate the persistence length from the exponential decay of the tangent—tangent correlation $\langle t_i \cdot t_0 \rangle = e^{(-l_i/l_{\rm p})}$. ²⁴ Here, t_i and t_0 are the tangents of two monomers separated by i steps along the chain, and l_i is the arc length between the ith and 0th monomer. We find the $l_{\rm p}$ of 3.8 nm for a P3HT melt at 600 K, comparable to the experimental value of 3.0 \pm 0.3 nm obtained by McCulloch et al.

2.1.2. Pure O-IDTBR. The crystal structure of O-IDTBR has been determined by Che et al. 32 We construct an initial state of 128 molecules of this crystal structure and equilibrate for 400 ns at 300 K and anisotropic pressure coupling of 1 atm. The system consists of 59 real atoms and 29 virtual sites per molecule. The details of constraints and potential parameters are listed in Section S4 of Supporting Information. We use the same time step (4 fs), thermostat, and barostat as given for P3HT simulation.

From the simulated crystal structure, we do not observe a significant change in density, and the crystal structure remains stable throughout simulation, as shown in Figure 3. The simulation box dimensions are shown in Table 2. The experimental density of crystalline O-IDTBR is 1243 kg/m³, which compares well to the simulated density of 1153 kg/m³.

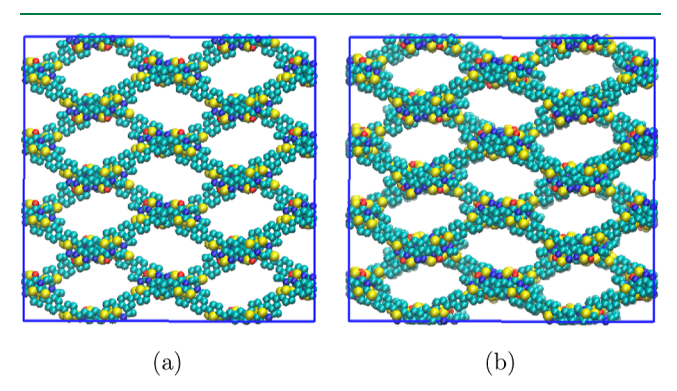


Figure 3. (a) Experimental and (b) simulated (400 ns) O-IDTBR crystal (side-groups not shown).

3. BLEND MORPHOLOGY

OPV efficiency depends on the local morphology of the donor—acceptor interface, at which excitons dissociate and produce current. Our virtual site coarse-graining approach enables simulations of realistic configurations of the blend at an atomistic scale. However, the system must be well equilibrated to obtain a realistic blend morphology. The most persuasive test of equilibration is to show that very different initial states produce the same equilibrated state. Therefore, we compare the equilibrated system obtained from two very different initial states—intimately mixed and completely demixed.

For an intimately mixed initial state, 90 molecules each of octamer P3HT and O-IDTBR are stacked alternatively in a simulation box (see Figure 4). This initial state is simulated for 3 ns while resizing to a near-melt density, followed by an NPT simulation for 600 ns at 600 K and 1 atm. For a demixed initial state, we simulate 180 molecules each of octamer P3HT and O-IDTBR, assembled by placing two equilibrated pure melts next to each other (see Figure 5). We equilibrate this initial state by simulating for 6 ns while resizing to a near-melt density, followed by 1500 ns of NPT simulation. During this NPT simulation, molecules diffuse across the simulation box as shown in Figure 5c. The 1500 ns coarse-grained simulation

runs in about 10 days, which would have taken several months for an all-atom simulation.

Comparing both simulations after 60 ns, as shown in Figures 4b and 5b, highlights the need for long simulations for these slow-relaxing systems. Both systems equilibrate to a homogeneous phase with no interface (see Figures 4c and 5c). Also, each system reaches the same energy per volume, indicating that they have equilibrated to the same state despite starting from a very different initial configuration.

The real P3HT/O-IDTBR BHJ uses P3HT chains much longer than our octamers; the resulting blends could certainly be immiscible, while our system may be miscible because of short P3HT chains. Here, we estimate the critical chain length required to observe phase separation in simulation.

For a polymer blend, the critical χ for demixing is given by ³³

$$\chi_{\rm c} = \frac{1}{2} \left(\frac{1}{\sqrt{N_{\rm A}}} + \frac{1}{\sqrt{N_{\rm B}}} \right)^2$$
(3)

where $N_{\rm A}$ and $N_{\rm B}$ are the number of monomers of polymers A and B, respectively. Our system of octamers P3HT and O-IDTBR consists of 24.4 and 21.6 "reference monomers" with a volume of 0.1 nm³ each, respectively. Therefore, the critical $\chi_{\rm c}$ equals 0.087 per 0.1 nm³ reference volume. From our simulation, we can readily obtain only the enthalpic contribution to χ from the energy difference between pure and mixed systems as

$$\chi_{\rm h} = \frac{\Delta H_{\rm m}}{kT\phi_1\phi_2} \tag{4}$$

which gives χ_h equal to 0.041, smaller than the critical value χ_c . If the entropic contribution to χ is negligible, we should not observe phase separation with our short octamer P3HT chains. If we assume $\chi = \chi_h$, then to observe phase separation, P3HT should consist of at least 197 reference monomers, corresponding to 64 3-hexyl thiophene repeat units or a molecular weight of 10.6 kg mol⁻¹.

Even if the entropic χ is such that the total χ slightly exceeds χ_c for our oligomers, we might still obtain a homogeneous system, if the equilibrium interface is too wide to fit in the simulation box. By this argument, we expect a real P3HT/O-IDTBR interface that must be greater than half of our simulation box size of 15.8 nm. Thus, our simulation may be regarded as representing a locally homogeneous portion of the donor–acceptor interface. If we could obtain a value of χ through experiment or simulation, we can estimate the interface profile using the Helfand–Tagami result.³⁴ In this study, we focus on the properties of the interfacial region as represented by our simulation.

3.1. Side-Group Effect on Morphology. Side-groups are electronically inactive parts of conjugated polymers; they are added to make the polymer soluble and play a critical role in determining the morphology. Here, we examine the effect of P3HT and O-IDTBR side-groups on local morphology, which we characterize with respect to the number of close contacts of a chain.

Table 2. O-IDTBR Crystal Structure Dimensions from Experiment and Simulation

dimension	а	ь	с	A	β	γ
experiment	13.7638	15.8480	32.7182	90.0000	96.8530	90.0000
simulation	15.1772	15.2840	33.1586	90.0580	97.0824	89.7299

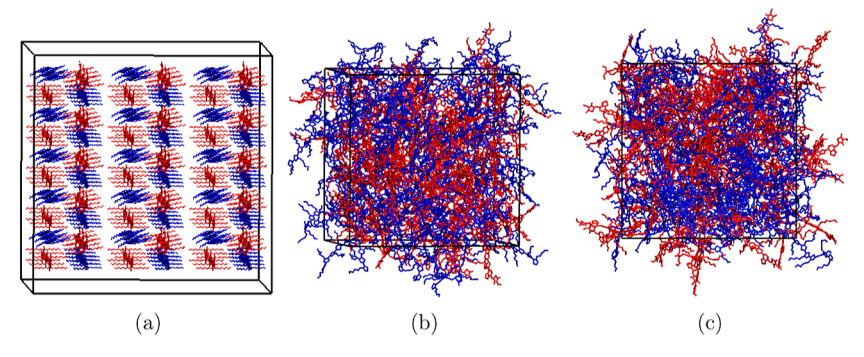


Figure 4. (a) Initial, (b) after 60 ns, and (c) equilibrated (600 ns) configurations of P3HT (blue) and O-IDTBR (red) in MD simulation with the intimately mixed initial condition.

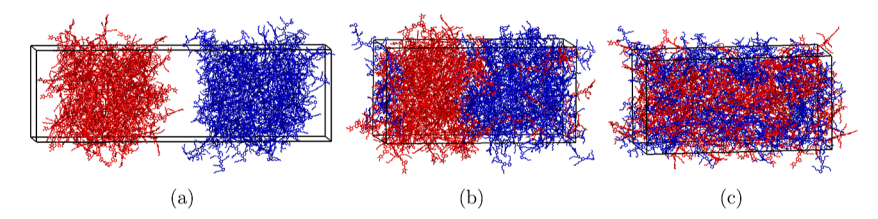


Figure 5. (a) Initial, (b) after 60 ns, and (c) equilibrated (1500 ns) configurations of P3HT (blue) and O-IDTBR (red) in MD simulation with the demixed initial condition.

Figure 6. (a) P3HT monomer and (b) O-IDTBR molecule with center of the conjugated ring shown in red.

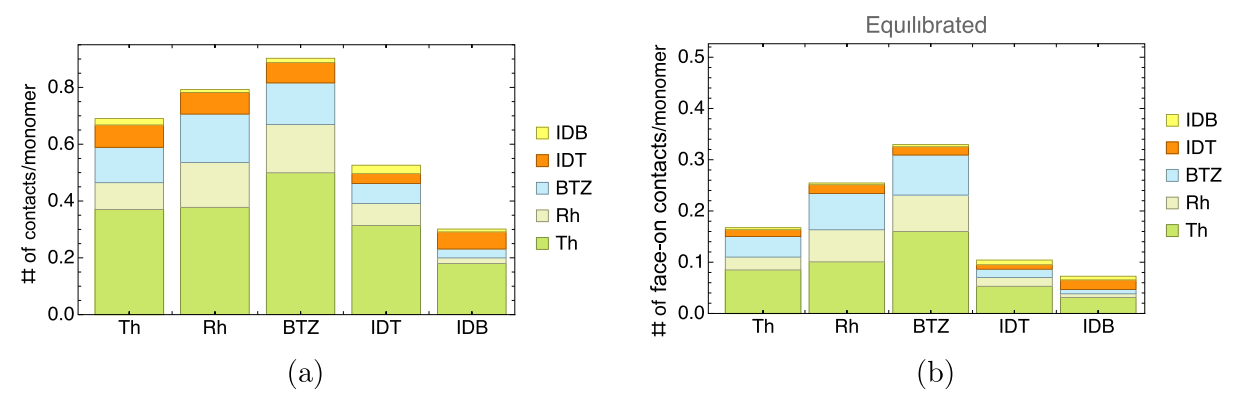


Figure 7. (a) Number of contacts/monomer and (b) number of face-on contacts/monomer in the equilibrated blend of P3HT/O-IDTBR.

Interchain electron transfer occurs between neighboring moieties in close proximity. The electronically active part of donor and acceptor molecules is conjugated moieties along the backbone. We define a "contact pair" between moieties when the distance between their geometric centers is less than 0.5 nm; a"face-on pair" is a contact pair in which two rings are parallel within $\pm 10^{\circ}$. To quantify local morphology relevant to carrier transport, we count the number of contact pairs and face-on pairs.

We label the P3HT monomer as "Th"; correspondingly, the moieties of O-IDTBR are labeled as "Rh" for rhodanine,

"BTZ" for benzothiadiazole, "IDT" for thiophene in the center moiety, and "IDB" for the phenyl ring, as shown in Figure 6.

The architectural details of solubilizing side-groups profoundly affect the number of close contacts of the attached moiety. In P3HT, the side-group is a flexible hexyl chain attached to each ring, as shown in Figure 6. The first side-group carbon attached to the ring is in the plane of the ring due to sp² hybridization. In O-IDTBR, two octyl side-groups are attached to the bridge carbons near the center of the molecule. The first carbon atom of each octyl side-group in O-IDTBR projects out of the backbone plane. As a result, close

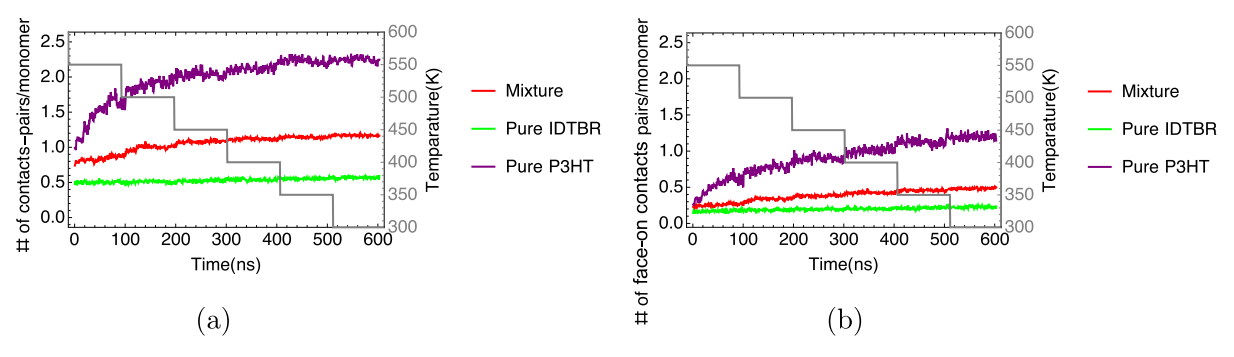


Figure 8. Total (a) number of contacts per monomer and (b) number of face-on contact per monomer as a function of annealing temperature and time

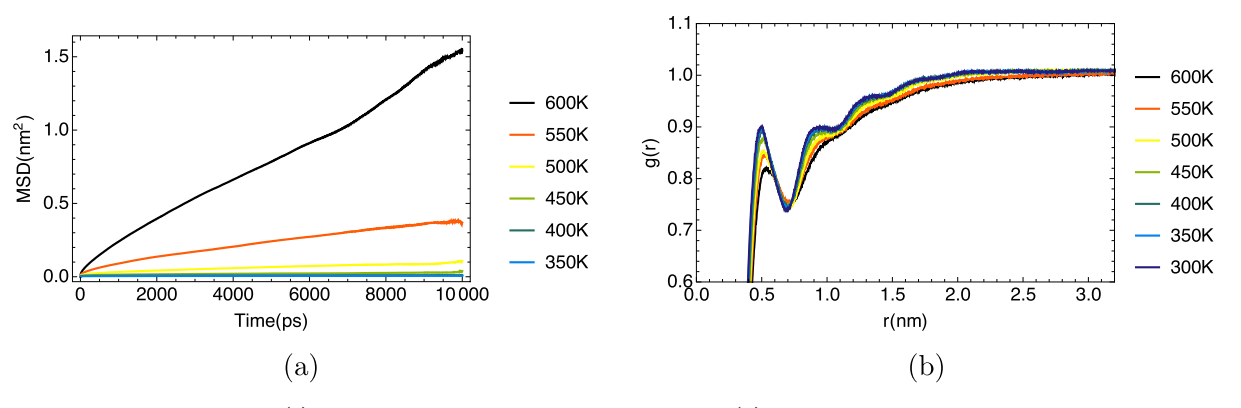


Figure 9. Effect of annealing on the (a) mean-square displacement of molecules and (b) radial distribution function of P3HT with respect to O-IDTBR in blend.

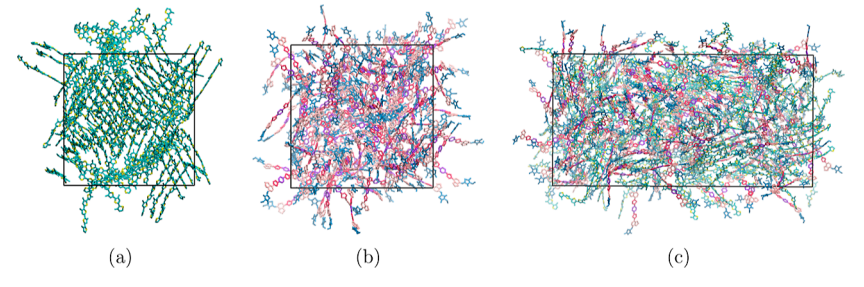


Figure 10. Snapshots of annealed (a) P3HT, (b) O-IDTBR, and (c) blend at 300 K (side-groups not shown).

contacts with central moieties on O-IDTBR are sterically hindered and should be less frequent than other moieties.

Figure 7 represents the total number of contacts and face-on contacts per monomer for all moieties in a P3HT/O-IDTBR blend. For each type of moiety, the number of contacts with other types of moieties is represented by the color-coded contribution to the total height of the bar. Contacts are most common for BTZ, to which no side-group is attached. Rh has an ethyl chain attached to its nitrogen atom and hence has a lower number of contacts per monomer than BTZ.

Although Th also has a side-group, it is attached in the backbone plane and does not hinder other monomers from approaching closely. Indeed, contacts with Th are most prevalent for all moieties. In contrast, the bulky side-group of O-IDTBR is attached to both sides of IDB, which effectively disrupts close contact with other monomers, especially with other IDB molecules. The IDT ring in O-IDTBR is also affected by the out-of-plane side-group but less severely than IDB. These results suggest that we can favor contacts with given moieties by engineering the side-group appropriately. In

this way, we can promote charge transfer or suppress charge recombination by promoting or preventing contacts between specific moieties.

3.2. Annealing Effect on Morphology. Capturing the effect of annealing in simulation is extremely challenging because polymer chains rearrange very slowly, especially at lower temperatures. However, the virtual-site coarse-graining enables us to explore annealing and quenching even in a chemically realistic system.

We study the effect of annealing on the local structures of pure P3HT, pure O-IDTBR, and an equimolar blend. We cool the system from 600 to 300 K in about 600 ns using the following protocol: we hold the temperature constant for 100 ns and drop it by 50 K in 1 ns to the next lower temperature, as shown in Figure 8.

As we slowly anneal the blend from 600 to 300 K, the molecular diffusivity decreases and is negligible below 500 K, as shown in Figure 9a. However, in Figure 9b, we observe the growth of peaks in the radial distribution function (RDF) of P3HT with respect to O-IDTBR even below 500 K. Although

molecules do not diffuse much, the RDF increases by local rearrangements.

Annealing affects the local structure of the two pure phases very differently from the mixed phase. The number of contacts in all three systems increases at different rates, as shown in Figure 8. Annealing O-IDTBR does not increase the number of contacts very much, primarily because of the large steric hindrance of the side-group. In contrast, the in-plane sidegroup on P3HT does not impede the π - π stacking; indeed, we observe some tendency to crystallize by annealing, as shown in Figure 10a. The crystallization in pure P3HT increases the number of contact pairs to two per monomer—each monomer has one monomer above and one below. In contrast, the number of contacts per monomer in the blend is lower than the average number of contacts for pure systems. As we anneal the mixture, the presence of O-IDTBR molecules disrupts the formation of $\pi - \pi$ stacking in P3HT, as shown in Figure 10c, so the number of contacts in the blend does not increase very much.

4. CONCLUSIONS

We have developed an efficient coarse-graining method to reduce the simulation time significantly while faithfully retaining the monomer structure and interactions. The resulting simulations are 10 times faster than an equivalent atomistic simulation and produce a realistic morphology for a P3HT/O-IDTBR blend. The octamers P3HT and O-IDTBR form a miscible blend in the simulation, suggesting an interface width greater than 7 nm even if these two materials phase separate in experiment.

Simulation results for pure O-IDTBR show that the bulky O-IDTBR side-group sterically hinders close contact with the IDB moiety. Hence, we speculate that most interchain charge transfer in these materials must be mediated by BTZ and Rh moieties. In contrast, simulations of pure P3HT show that the in-plane side-group of P3HT provides little steric hindrance for close contacts, which facilitates better interchain charge transfer.

Here, we also demonstrate that annealing increases the number of contacts per monomer, more so in pure P3HT than in pure O-IDTBR, because pure P3HT tends to crystallize within the timescale of our simulations. In the blend, O-IDTBR hinders $\pi - \pi$ stacking of P3HT, thereby frustrating both crystallization and close contacts.

ASSOCIATED CONTENT

Supporting Information

The Supporting Information is available free of charge at https://pubs.acs.org/doi/10.1021/acs.jctc.2c00470.

Description of the method to create the monomer.itp file and the monomer.pdb file and lists of P3HT potential parameters and O-IDTBR potential parameters (PDF)

AUTHOR INFORMATION

Corresponding Author

Scott T. Milner — Department of Chemical Engineering, The Pennsylvania State University, University Park, Pennsylvania 16802, United States; Department of Materials Science and Engineering, The Pennsylvania State University, University Park, Pennsylvania 16802, United States; orcid.org/0000-0002-9774-3307; Email: stm9@psu.edu

Authors

Puja Agarwala — Department of Chemical Engineering, The Pennsylvania State University, University Park, Pennsylvania 16802, United States; orcid.org/0000-0003-3561-6633

Enrique D. Gomez — Department of Chemical Engineering, The Pennsylvania State University, University Park, Pennsylvania 16802, United States; Department of Materials Science and Engineering and Materials Research Institute, The Pennsylvania State University, University Park, Pennsylvania 16802, United States; orcid.org/0000-0001-8942-4480

Complete contact information is available at: https://pubs.acs.org/10.1021/acs.jctc.2c00470

Notes

The authors declare no competing financial interest.

ACKNOWLEDGMENTS

Financial support from the National Science Foundation (DMREF-1921854) and Office of Naval Research (N00014-19-1-2453) is acknowledged.

REFERENCES

- (1) Norton, B.; Eames, P. C.; Mallick, T. K.; Huang, M. J.; McCormack, S. J.; Mondol, J. D.; Yohanis, Y. G. Enhancing the performance of building integrated photovoltaics. *Sol. Energy* **2011**, *85*, 1629–1664.
- (2) Lipomi, D. J.; Bao, Z. Stretchable, elastic materials and devices for solar energy conversion. *Energy Environ. Sci.* **2011**, *4*, 3314–3328.
- (3) Kaltenbrunner, M.; White, M. S.; Głowacki, E. D.; Sekitani, T.; Someya, T.; Sariciftci, N. S.; Bauer, S. Ultrathin and lightweight organic solar cells with high flexibility. *Nat. Commun.* **2012**, *3*, 770.
- (4) Hoppe, H.; Sariciftci, N. S. Morphology of polymer/fullerene bulk heterojunction solar cells. *J. Mater. Chem.* **2006**, *16*, 45–61.
- (5) Schwartz, B. J. Conjugated polymers as molecular materials: How chain conformation and film morphology influence energy transfer and interchain interactions. *Annu. Rev. Phys. Chem.* **2003**, *54*, 141–172.
- (6) Zimmerman, J. D.; Xiao, X.; Renshaw, C. K.; Wang, S.; Diev, V. V.; Thompson, M. E.; Forrest, S. R. Independent control of bulk and interfacial morphologies of small molecular weight organic heterojunction solar cells. *Nano Lett.* **2012**, *12*, 4366–4371.
- (7) Chen, X.-K.; Qian, D.; Wang, Y.; Kirchartz, T.; Tress, W.; Yao, H.; Yuan, J.; Hülsbeck, M.; Zhang, M.; Zou, Y.; Sun, Y.; Li, Y.; Hou, J.; Inganäs, O.; Coropceanu, V.; Bredas, J.-L.; Gao, F. A unified description of non-radiative voltage losses in organic solar cells. *Nat. Energy* **2021**, *6*, 799–806.
- (8) Yan, J.; Rezasoltani, E.; Azzouzi, M.; Eisner, F.; Nelson, J. Influence of static disorder of charge transfer state on voltage loss in organic photovoltaics. *Nat. Commun.* **2021**, *12*, 3642.
- (9) Burke, T. M.; McGehee, M. D. How high local charge carrier mobility and an energy cascade in a three-phase bulk heterojunction enable >90% quantum efficiency. *Adv. Mater.* **2014**, *26*, 1923–1928.
- (10) Liu, T.; Gao, W.; Wang, Y.; Yang, T.; Ma, R.; Zhang, G.; Zhong, C.; Ma, W.; Yan, H.; Yang, C. Unconjugated Side-Chain Engineering Enables Small Molecular Acceptors for Highly Efficient Non-Fullerene Organic Solar Cells: Insights into the Fine-Tuning of Acceptor Properties and Micromorphology. *Adv. Funct. Mater.* **2019**, 29, 1902155.
- (11) Cheng, P.; Yang, Y. Narrowing the band gap: the key to high-performance organic photovoltaics. *Acc. Chem. Res.* **2020**, *53*, 1218–1228
- (12) Cao, W.; Xue, J. Recent progress in organic photovoltaics: device architecture and optical design. *Energy Environ. Sci.* **2014**, *7*, 2123–2144.

- (13) Kuei, B.; Gomez, E. D. Chain conformations and phase behavior of conjugated polymers. *Soft Matter* **2017**, *13*, 49–67.
- (14) Li, Q.; Wang, L.-M.; Liu, S.; Zhan, X.; Zhu, T.; Cao, Z.; Lai, H.; Zhao, J.; Cai, Y.; Xie, W.; Huang, F. Impact of Donor-Acceptor Interaction and Solvent Additive on the Vertical Composition Distribution of Bulk Heterojunction Polymer Solar Cells. ACS Appl. Mater. Interfaces 2019, 11, 45979–45990.
- (15) Gurney, R. S.; Lidzey, D. G.; Wang, T. A review of non-fullerene polymer solar cells: from device physics to morphology control. *Rep. Prog. Phys.* **2019**, *82*, 036601.
- (16) Cates, N.; Cho, E.; Junk, M. J. N.; Gysel, R.; Risko, C.; Kim, D.; Sweetnam, S.; Miller, C. E.; Richter, L. J.; Kline, R. J.; Heeney, M.; McCulloch, I.; Amassian, A.; Acevedo-Feliz, D.; Knox, C.; Hansen, M. R.; Dudenko, D.; Chmelka, B. F.; Toney, M. F.; Brédas, J.-L.; McGehee, M. D. Use of X-Ray Diffraction, Molecular Simulations, and Spectroscopy to Determine the Molecular Packing in a Polymer-Fullerene Bimolecular Crystal. *Adv. Mater.* **2012**, 24, 6071–6079.
- (17) Jackson, N. E. Coarse-Graining Organic Semiconductors: The Path to Multiscale Design. *J. Phys. Chem. B* **2020**, *125*, 485–496.
- (18) Huang, D. M.; Faller, R.; Do, K.; Moulé, A. J. Coarse-grained computer simulations of polymer/fullerene bulk heterojunctions for organic photovoltaic applications. *J. Chem. Theory Comput.* **2010**, *6*, 526–537.
- (19) Curcó, D.; Alemán, C. Computational tool to model the packing of polycyclic chains: Structural analysis of amorphous polythiophene. *J. Comput. Chem.* **2007**, *28*, 1743–1749.
- (20) Kupgan, G.; Chen, X.-K.; Brédas, J.-L. Molecular packing in the active layers of organic solar cells based on non-fullerene acceptors: Impact of isomerization on charge transport, exciton dissociation, and nonradiative recombination. ACS Appl. Energy Mater. 2021, 4, 4002—4011.
- (21) Root, S. E.; Savagatrup, S.; Pais, C. J.; Arya, G.; Lipomi, D. J. Predicting the mechanical properties of organic semiconductors using coarse-grained molecular dynamics simulations. *Macromolecules* **2016**, 49, 2886–2894.
- (22) Jankowski, E.; Ellyson, N.; Fothergill, J. W.; Henry, M. M.; Leibowitz, M. H.; Miller, E. D.; Alberts, M.; Chesser, S.; Guevara, J. D.; Jones, C. D.; Klopfenstein, M.; Noneman, K. K.; Singleton, R.; Uriarte-Mendoza, R. A.; Thomas, S.; Estridge, C. E.; Jones, M. L. Perspective on coarse-graining, cognitive load, and materials simulation. *Comput. Mater. Sci.* **2020**, *171*, 109129.
- (23) Brédas, J.-L.; Beljonne, D.; Coropceanu, V.; Cornil, J. Charge-Transfer and Energy-Transfer Processes in π -Conjugated Oligomers and Polymers: A Molecular Picture. *Chem. Rev.* **2004**, *104*, 4971–5004.
- (24) Zhang, W.; Gomez, E. D.; Milner, S. T. Predicting chain dimensions of semiflexible polymers from dihedral potentials. *Macromolecules* **2014**, *47*, 6453–6461.
- (25) Zhan, P.; Zhang, W.; Jacobs, I. E.; Nisson, D. M.; Xie, R.; Weissen, A. R.; Colby, R. H.; Moulé, A. J.; Milner, S. T.; Maranas, J. K.; Gomez, E. D. Side chain length affects backbone dynamics in poly(3-alkylthiophene)s. *J. Polym. Sci., Part B: Polym. Phys.* **2018**, *56*, 1193–1202.
- (26) McCulloch, B.; Ho, V.; Hoarfrost, M.; Stanley, C.; Do, C.; Heller, W. T.; Segalman, R. A. Polymer Chain Shape of Poly(3-alkylthiophenes) in Solution Using Small-Angle Neutron Scattering. *Macromolecules* **2013**, *46*, 1899–1907.
- (27) Verploegen, E.; Mondal, R.; Bettinger, C. J.; Sok, S.; Toney, M. F.; Bao, Z. Effects of Thermal Annealing Upon the Morphology of Polymer-Fullerene Blends. *Adv. Funct. Mater.* **2010**, *20*, 3519–3529.
- (28) Savikhin, V.; Jagadamma, L. K.; Purvis, L. J.; Robertson, I.; Oosterhout, S. D.; Douglas, C. J.; Samuel, I. D.; Toney, M. F. Morphological, chemical, and electronic changes of the conjugated polymer PTB7 with thermal annealing. *IScience* **2018**, *2*, 182–192.
- (29) Van Der Spoel, D.; Lindahl, E.; Hess, B.; Groenhof, G.; Mark, A. E.; Berendsen, H. J. GROMACS: fast, flexible, and free. *J. Comput. Chem.* **2005**, 26, 1701–1718.

- (30) Jorgensen, W. L.; Madura, J. D.; Swenson, C. J. Optimized intermolecular potential functions for liquid hydrocarbons. *J. Am. Chem. Soc.* **1984**, *106*, 6638–6646.
- (31) Bombile, J. H.; Shetty, S.; Janik, M. J.; Milner, S. T. Polaron hopping barriers and rates in semiconducting polymers. *Phys. Chem. Phys.* **2020**, 22, 4032–4042.
- (32) Che, Y.; Zhang, Y.; Yang, Y.; Liu, C.-H.; Izquierdo, R.; Xiao, S. S.; Perepichka, D. F. Understanding the Photovoltaic Behavior of AD-A Molecular Semiconductors through a Permutation of End Groups. J. Org. Chem. 2019, 85, 52–61.
- (33) Rubinstein, M.; Colby, R. H. Polymer Physics; Oxford University Press: New York, 2003; Vol. 23.
- (34) Helfand, E.; Tagami, Y. Theory of the interface between immiscible polymers. II. J. Chem. Phys. 1972, 56, 3592–3601.

□ Recommended by ACS

Development and Testing of an All-Atom Force Field for Diketopyrrole Polymers with Conjugated Substituents

Vivek Sundaram, Björn Baumeier, et al.

NOVEMBER 19, 2020

THE JOURNAL OF PHYSICAL CHEMISTRY B

READ 🖸

Design Principles for the Acceptor Units in Donor-Acceptor Conjugated Polymers

Tuba Hacıefendiolu and Erol Yildirim

OCTOBER 18, 2022

ACS OMEGA

READ 🗹

Imaging 0.36 nm Lattice Planes in Conjugated Polymers by Minimizing Beam Damage

Brooke Kuei, Enrique D. Gomez, et al.

SEPTEMBER 22, 2020

MACROMOLECULES

READ [7

Multi-Edge Resonant Tender X-ray Diffraction for Probing the Crystalline Packing of Conjugated Polymers

Guillaume Freychet, Christopher R. McNeill, et al.

MAY 26, 2022

MACROMOLECULES

READ 🗹

Get More Suggestions >